Journal of Materials Chemistry A

PAPER

View Article Online
View Journal | View Issue

Cite this: J. Mater. Chem. A, 2017, 5, 8477

A highly stable polyoxometalate-based metal–organic framework with π–π stacking for enhancing lithium ion battery performance†

Qing Huang,‡ Tao Wei,‡ Mi Zhang, Long-Zhang Dong, A-Man Zhang, Shun-Li Li, Wen-Jing Liu, Jiang Liu and Ya-Qian Lan*

Received 27th January 2017
Accepted 6th April 2017

DOI: 10.1039/c7ta00900c

rsc.li/materials-a

A novel polyoxometalate-based metal–organic framework (POMOF), $[PMo_8^{V}Mo_4^{VI}O_{37}(OH)_3Zn_4][TPT]_5\cdot 2TPT\cdot 2H_2O$ (**NNU-11**, TPT = tris-(4-pyridyl)triazine), was synthesized. Zn-ε-Keggin fragments were directly connected with TPT ligands generating 2D layers and further interdigitated with each other by π–π stacking interactions to pack into a 3D array. The compound exhibited excellent stability in air and different organic solvents and even in different pH (pH 1–11) aqueous solutions. It can be utilized as an anode material for lithium ion batteries (LIBs) due to the combination of the multi-electron redox property of POM units and the functionalization of MOFs. **NNU-11** exhibited a highly reversible capacity of 750 mA h g^{-1} at a current density of 50 mA g^{-1} after 200 cycles along with excellent cycle stability and rate performance. More importantly, for the first time, we designed and synthesized a POMOF crystalline structure model supported by π–π stacking interactions to demonstrate that intermolecular π–π stacking interactions are beneficial to promote the performance of LIBs.

Introduction

Electrical energy storage materials are potential substitutes for fossil fuels in the future and gain a high position due to their special advantages including low cost, excellent rechargeability, and environmental friendliness.[1] In addition to the above-mentioned characteristics, given the relatively high energy density and cycle life, lithium ion batteries (LIBs) have been one of the major electrical energy storage materials[2] and have attracted increasing research interests.[3] However, traditional graphite based anodes exhibit low practical capacity and poor rate capability, which still hampers their further development to meet higher demand of applications.[4] As a consequence, the exploitation of high rate capability and high capacity anode materials are highly desirable to LIBs. Enormous efforts have thus been dedicated to developing new anode materials for LIBs.[5]

Metal–organic frameworks (MOFs) are a versatile class of porous materials fabricated by bridging metals with organic linkers.[6] MOFs have been studied extensively in separation,[7] catalysis,[8] gas storage,[9] sensors,[10] and electrochemistry[3a,11] due to their remarkable surface areas and tunable porosities. Gradually, MOFs acting as LIBs anode materials have attracted increasing research interests. In 2006, Li *et al.* presented a new and exciting idea for the research of LIBs to exploit new MOF-based anode materials.[12] Since then, several other pristine MOFs were developed that enabled some progress in exploring anode materials for LIBs.[13] MOFs possess high surface areas and intrinsic permanent pores to capture Li^+ ions and provide channels for Li^+ ions, which are favorable for insertion-type reactions of LIBs. In addition, MOFs with appropriate metal centers and organic linkers provide advantages toward conversion-type reactions of LIBs. However, several MOFs did not exhibit high performance because of two major challenges faced: the valence change of transition metals is small and most MOFs are poor conductors of electricity.

Polyoxometalates (POMs), as a good anion cluster, are composed of multiple transition metals attached to oxygen atoms. POMs with oxygen-rich surfaces, tunable compositions, fascinating structures and being multi-electron redox active systems have led to their wonderful performance in catalysis,[14] magnetism[15] and LIBs.[16] For instance, $[PMo_{12}O_{40}]^{3-}$, endowed as an "electron sponge", exhibits a high capacity in LIBs due to the multi-electron reversible transfer.[16a] Nevertheless, several POMs possess good solubility in most solvents, which has limited their extensive development in LIBs. In order to make good use of the multi-electron reversible transfer property for meeting the first challenge of MOF in LIBs, POMs can be employed in constructing POMOFs, which is propitious to immobilize POMs as inorganic building blocks and maintain

Jiangsu Collaborative Innovation Centre of Biomedical Functional Materials, Jiangsu Key Laboratory of New Power Batteries, School of Chemistry and Materials Science, Nanjing Normal University, Nanjing 210023, Jiangsu, P. R. China. E-mail: yqlan@njnu.edu.cn

† Electronic supplementary information (ESI) available: Supplementary structural figures, IR, TG, XPS, ESI. CCDC 1524662 and 1524663. For ESI and crystallographic data in CIF or other electronic format see DOI: 10.1039/c7ta00900c

‡ These authors contributed equally.

the stability of POMOF networks in electrolyte. Moreover, the significant stability of their frameworks is in favor of reversible processes of lithium storage and generating high rate capability. Therefore, combining the advantages of MOFs and POMs to fabricate POMOFs as anode materials may promote the performance of LIBs. However, the synthesis of POMOF materials with appropriate organic ligands and POMs, particularly with good capability in LIBs, still remains a significant challenge. Therefore, few studies on POMOF materials that can be utilized as anode materials of LIBs have been investigated.[17]

In this study, we designed and synthesized an ultra-stable POMOF crystalline model supported by π–π stacking interactions. The crystalline POMOF are connected by tris(4-pyridyl) triazine (TPT) linkers to {ε-$PMo_8^{V}Mo_4^{VI}O_{40}Zn_4$} (Zn-ε-Keggin)[11b] units by an *in situ* method under hydrothermal conditions. The Zn-ε-Keggin unit was introduced into this study because of its excellent characteristics. On the one hand, the Zn-ε-Keggin is embedded by four Zn^{2+} located in a regular tetrahedral arrangement, which offers a 4-connected mode to form interesting structures with outstanding stability. On the other hand, the Zn-ε-Keggin, containing eight Mo^{V} and four Mo^{VI}, possess the important feature of multi-electron reversible transfer. Thus, the Zn-ε-Keggin with such excellent characteristics shows great promise as a part of an anode material for LIBs. In the light of a recent report,[18] these results clearly revealed that the π–π stacking of the framework affords an electron conduction path, which is conducive to strengthen the conductive capability for solving the problems arising due to MOFs being poor conductors of electricity. The TPT ligand, as we know, is an ideal candidate for the design and formation of the π–π stacking.[19] As a consequence, to obtain POMOF crystalline materials as anode materials with a high electrical conductivity for LIBs, we employed the TPT ligand as the linker to generate the π–π stacking with an electron conduction path. Currently, we focused more on the design and synthesis of POMOF materials with the π–π stacking as anode materials with excellent performance for LIBs and successfully isolated **NNU-11** as we expected. Furthermore, the battery performance of as-synthesized **NNU-11** toward LIBs was examined. As a novel anode material of LIBs, it showed an initial discharge capacity of 1200 mA h g^{-1} and a reversible capacity of 750 mA h g^{-1} for 200 cycles at 50 mA g^{-1}. For comparison, the LIBs behaviors of TPT and **NNU-12** containing Zn-ε-Keggin fragments were also tested under similar conditions. Moreover, for the first time, we employed a pristine crystalline structure model to demonstrate that the intermolecular π–π stacking interactions are propitious to improve the performance of LIBs.

Results and discussion

Single-crystal X-ray diffraction analysis indicated that **NNU-11** crystallizes in the space group of *P*2/*n*. The asymmetric unit consists of one [ε-$PMo_8^{V}Mo_4^{VI}O_{37}(OH)_3Zn_4$], three coordinated TPT ligands, one free TPT ligand and other guest molecules (Fig. 1a). The ε-Keggin unit decorated with four Zn(II) ions is different from the classical ε-Keggin-type. Each Zn(II) ion is embedded in a vacant position *via* its coordination to three

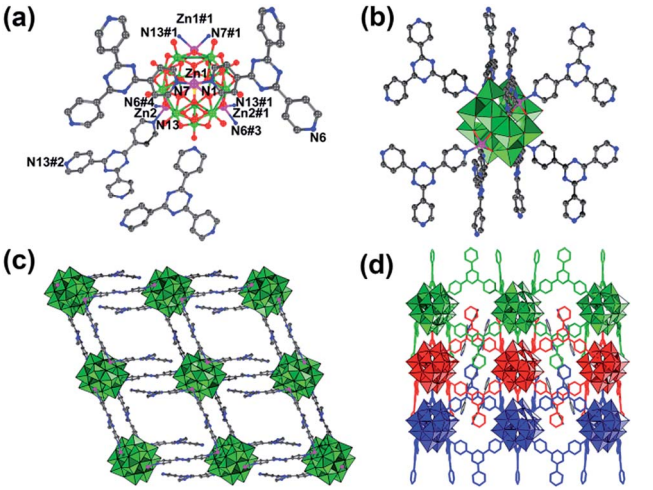

Fig. 1 Summary of the structure of **NNU-11**: (a) coordination environments for the Zn(II) centers in **NNU-11**. Color code: C, black; N, blue; O, red; Zn, pink; Mo, green; P, yellow. Symmetry codes: #1 0.5 − *x*, *y*, 0.5 − *z*; #2 1.5 − *x*, *y*, 0.5 − *z*; #3 −*x*, 1 − *y*, −*z*; #4 0.5 + *x*, 1 − y, 0.5 + *z*. (b) Connection mode between the Zn-ε-Keggin and TPT fragments; (c) view along the *b* axis of the 2D layer structure of **NNU-11**; (d) π–π stacking for supporting the 3D structure.

bridging O atoms of the ε-Keggin unit, which forms a tetrahedral structure. In addition to the three bridging O atoms, all the four embedded Zn(II) ions also coordinate to two N donors from two TPT ligands in **NNU-11**. The four Zn(II) ions can be categorized into two different types including Zn1 ion and Zn2 ion. Zn1 ion is bonded to two N atoms (N7 and N1) (Fig. 1a) from one TPT-1 ligand and one TPT-2 linker (Fig. S1†), but Zn2 ion is defined by two N atoms (N13 and N6#4) from two TPT-2 linkers. Therefore, each ε-Keggin subunit is attached by two TPT-1 ligands and six TPT-2 linkers (Fig. 1b). These tridentate ligands do not make full use of all three N coordination sites. For example, TPT-2 linkers acting as the bi-dentate linkages, utilize the two N atoms to connect two adjacent Zn-ε-Keggin subunits in order to form a square 2D layer with a $4^4 \cdot 6^2$ ***sql*** 4-connected uninodal net (Fig. 1c and S2†). Every TPT-1 ligand only employs one N atom to graft the Zn1 ion. TPT-1 ligands also play an indispensable role in every π–π interaction occurring between triazine rings from adjacent layers with centroid–centroid distance being 3.479 Å (Fig. 4a). As we can see, these 2D layers are further interdigitated with each other by π–π stacking interactions to pack to a 3D array, and the pore channels are occupied by bulky TPT guests (Fig. 1d, 4b and S3b†). In addition, we can clearly observe the π–π stacking interactions in different directions and angles (Fig. S3†). Furthermore, π–π interactions are also observed between the two triazine rings from TPT-1 ligands and the uncoordinated TPT molecules with centroid–centroid distance being 4.745 Å (Fig. 4a). Due to the π–π stacking interactions, the uncoordinated TPT molecules acting as guests are occupied in a gap between the layers, while two free TPT guest molecules interact by the π–π stacking interaction at a distance of 3.597 Å (Fig. 4a).

The purity of **NNU-11** was determined by comparing their simulated and as-synthesized samples by powder X-ray

diffraction (PXRD) analysis (Fig. 2). To examine the stability of pH, the as-synthesized sample was immersed in aqueous HCl or NaOH solutions at different pH values ranging from 1 to 11. After 24 hours, it was observed that the sample could still maintain its crystallinity and the color of the aqueous solutions was the same as the initial solutions. Comparing the PXRD patterns of the soaked crystals with the sample before the test, it was found that only the peak intensities showed a change, with no other significant changes for each tested sample, confirming their excellent stability with pH (Fig. 2a). Due to the relatively small pores and the synthetic method of acid system under hydrothermal conditions, **NNU-11** exhibited not only good stability in different acidic and basic solutions but also in DMF, DMA and the electrolyte used for LIBs (Fig. 2b). The excellent chemical stability is beneficial for studying the cycle life of lithium ion batteries. **NNU-11** was ground and spread on Cu foils; it was subjected to a pressure of 2.5 MPa, similar to that of working electrode of LIBs. The resulting sample (**NNU-11**) eventually exhibited a good mechanical stability (Fig. S4†). It also exhibited a good framework stability after the loss of crystal water molecules (Fig. S5†). The thermal stability of **NNU-11** was evaluated by thermogravimetric analysis (TGA) in O_2 atmosphere (Fig. S6†). The weight loss step ranged from 310 °C to 480 °C, which signified the decomposition of all guest molecules and organic ligands. The final residue contained ZnO and MoO_3.

The electrochemical performance of **NNU-11** was evaluated by assembling it into coin cells with lithium as the counter electrode and cycling between 3.0 and 0.01 V *vs.* Li^+/Li. Fig. 3c shows the cycling performances of **NNU-11** at a current density of 50 mA g^{-1}. The charge/discharge profiles of the **NNU-11** anode for cycle number of 1, 2, 50 and 100 are displayed in Fig. 3a, and the first discharge and charge capacities of **NNU-11** were 1322.3 and 810.6 mA h g^{-1}, which obtained an initial coulombic efficiency (CE) of 61.3%. The initial irreversible capacity loss is largely ascribed to the decomposition of the electrolyte and subsequent formation of the solid electrolyte interphase (SEI) film. Cyclic voltammetry (CV) results in the range of 0.01–3.0 V at a scan rate of 0.2 mV s^{-1} for the first 3 cycles are illustrated in Fig. 3b. In the first discharge, a broad cathodic peak at about 0.6 V, which often was found, is attributed to the SEI formation. In the subsequent cycles, two indistinct peaks became visible at a potential of 1.1 V for the reduction and 1.25 V for the oxidation, indicating an electrochemical process, which may be ascribed to the reduction and oxidation of the Mo and Zn of **NNU-11**. After the first cycle, the curves almost overlapped, which indicates a good electrochemical reversibility of the electrode due to the formation of a stable SEI film.

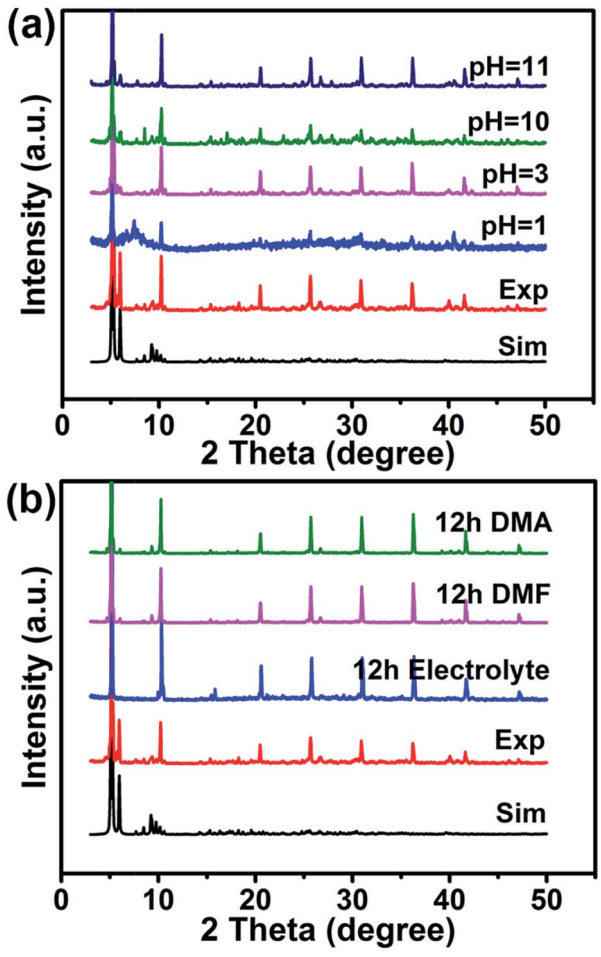

Fig. 2 PXRD patterns of **NNU-11**: (a) the as-synthesized sample soaked in aqueous solutions with different pH values at room temperature for 24 h and (b) immersed in electrolyte and other organic solvents at room temperature for 12 h. "Sim": simulated pattern, and "Exp": as-synthesized sample.

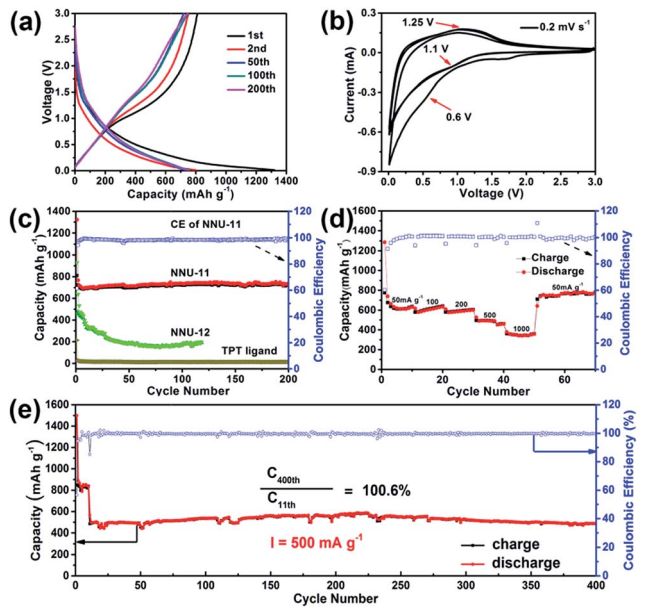

Fig. 3 Electrochemical performance of **NNU-11**: the specific capacity was calculated based on the mass of active material. (a) Charge/discharge profiles for different cycles constantly at 50 mA g^{-1}. (b) CV profiles at a scan rate of 0.2 mV s^{-1}. (c) Cycling performance at a current density of 50 mA g^{-1}. (d) Cycling at various current densities. (e) Cycle performance at a current density of 500 mA g^{-1} (50 mA g^{-1} was used for activation in the first 10 cycles).

As seen in Fig. 3c, after the first few cycles, the CE of **NNU-11** quickly improved to above 99%. After 200 cycles, the reversible capacity of **NNU-11** was stabilized at 750 mA h g^{-1}, it demonstrated excellent cycling stability. This ultra-stability may benefit from the open framework of MOFs that could mechanically buffer the volume change of the POMs and prevent the POMOFs particles from separating from the electrode, thus eventually leading to its cycling stability. To investigate the influences of the Zn-ε-Keggin fragments and the TPT ligands in LIBs, **NNU-12** and TPT acting as anode materials were also examined respectively under similar conditions. **NNU-12** $\{[PMo_8{}^{V}Mo_4{}^{VI}O_{36}(OH)_4Zn_4][BCPT]_2 \cdot x\text{Guests}\}$ was formed by POM units and organic ligands, whose 3D nets with ***dia*** topology were generated by both Zn-ε-Keggin fragments and $BCPT^{2-}$ linkers (Fig. S7†). TGA, IR, and PXRD images of **NNU-12** are exhibited in ESI (Fig. S6, S8, S9 and S10†). Although **NNU-12** contained the same Zn-ε-Keggin POM units as **NNU-11**, the reversible capacity of **NNU-12** was only about 200 mA h g^{-1} and close to the theoretical capacity (≈238 mA h g^{-1}). The TPT ligand almost had no contribution to the capacity (Fig. 3c). However, when **NNU-11** was formed by the Zn-ε-Keggin blocks and the TPT ligands, a special structure with the π–π stacking interactions was formed, which exhibited excellent performance in LIBs. The π–π stacking interactions in **NNU-11** have two functions: first, it can greatly increase the electron conductivity, which can effectively reduce the ohmic loss of the batteries; second, the pseudocapacitance can be achieved by the storage of Li^+ between the layers supported by π–π stacking (see in details below). Thus, the comparison results demonstrated that the π–π stacking interactions are conducive to improving LIBs capacity. The capacity of **NNU-11** is also higher than that of other pristine (not used as a template, such as carbonation) POMOFs or MOFs anodes that have been reported (Table S1†).

To further investigate the reaction mechanism of LIBs, the element compositions and valences of **NNU-11** before the test and after discharging at 0.01 V were observed by the X-ray photoelectron spectroscopy (XPS). The survey spectrums of both the samples demonstrated the existence of C, Zn, Mo, P and O elements (Fig. S11†). Before the test, the C 1s XPS spectrum were deconvoluted into C–C (284.8 eV), C–N (285.3 eV) and C=C (286.5 eV)[20] (Fig. S11b†). After discharging to 0.01 V, the C=C peak disappeared and a C=O peak appeared because of the insertion of Li^+ and the formation of the SEI film (the main composite is Li_2CO_3) (Fig. S11f†). Therefore, all the uncoordinated N of pyridine of **NNU-11**, which could capture the Li^+, likely took part in Li insertion. In addition, the Mo 3d spectrum of **NNU-11** before the test had the two main peaks at 232.3 eV and 235.5 eV (Fig. S11c†), which could be assigned to Mo^{6+} 3d5/2 and Mo^{6+} 3d3/2 of MoO_3, respectively.[21] After discharging to 0.01 V, parts of Mo^{6+} were reduced to Mo^{4+} as observed from the appearance of Mo^{4+} peaks at a binding energy of 232.8 eV (Fig. S11g†).[22] As can be seen in Fig. S11d,† the Zn 2p spectra has two main peaks of Zn 2p3/2 and Zn 2p1/2, and demonstrates the existence of Zn^{2+}, whereas the contribution at higher BE (≈1021.1 eV) is assigned to Zn^0 when discharged to 0.01 V (Fig. S11h†).[23] Thus, as in the case of most conversion mechanisms, the valence change of both Mo and Zn also indicated the redox reaction occurring in LIBs.

Interestingly, 750 mA h g^{-1} is much higher than the theoretical capacity of **NNU-11** (≈230 mA h g^{-1}), which is based on the following aspects: (1) redox reactions of metal ions in Zn-ε-Keggin (Zn^{2+} to Zn and Mo^{6+} to Mo^{4+});[16a,24] (2) possible lithiation/delithiation sites for coordination with Li in the organic ligands, such as uncoordinated N (Fig. 4c). The access capacity here may be caused by the storage of Li^+ between the layers supported by π–π stacking. To confirm whether the capacity is contributed by the capacitive behavior or not, the CV profiles of **NNU-11** at different scan rates (0.2–10 mV s^{-1}) were recorded between 0.01–3.0 V (Fig. 4d); the power law $i = av^b$, where v represents the scan rate, and a and b are alterable parameters can be utilized to explain this.[25] In general, when $b = 0.5$, it means that the electrode reaction is diffusion-controlled and satisfies Cottrell's equation: $i = av^{0.5}$. For the reaction that is limited by a surface process, $b = 1$. The parameter b can be determined by the slope of the linear plot of log i *versus* log v. It is worth noting that when the scan rate was increased from 0.2 to 10 mV s^{-1}, the b value at 1.2 V was determined to be 0.75, which indicated contributions from both, and the b value was 0.96 at 0.1 V, which revealed a surface-

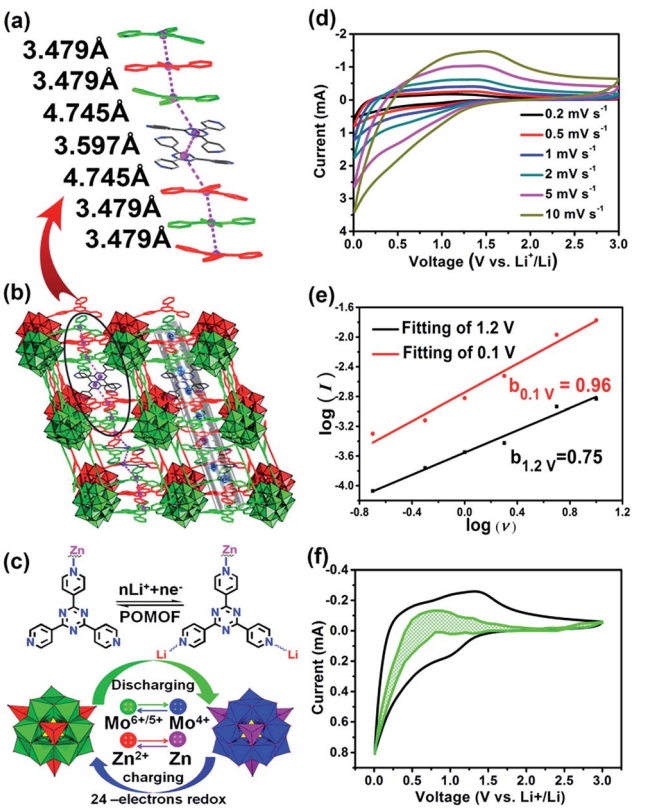

Fig. 4 (a) The detailed information about π–π stacking. (b) π–π stacking interactions between adjacent layers. (c) The schematic diagram of the possible mechanism for the capacity of **NNU-11**. (d) CV curves of **NNU-11** at various scan rates from 0.2 to 10 mV s^{-1}. (e) *b*-Value determination of 1.2 V and 0.1 V cathodic current. (f) Capacitive-controlled charge storage contributions separated with cyclic voltammograms at 0.5 mV s^{-1} scan.

controlled charge storage behavior (Fig. 4e). With this in mind, we can write the equations below (eqn (1) or (2)), *i.e.*, the current response "*i*" at a given potential "*v*" is the sum of two contributions supported by the capacitance and intercalation capacity.[25b–d]

$$i(V) = k_1 v + k_2 v^{0.5} \quad (1)$$

or

$$i(V)/v^{0.5} = k_1 v^{0.5} + k_2 \quad (2)$$

where $k_1 v$ and $k_2 v^{0.5}$ is assigned to the current contributions from the capacitive and diffusion processes (intercalation), respectively. Therefore, the current response due to diffusion and capacitive processes at a given potential can be determined by k_1 and k_2. In Fig. 4f, the green shaded area indicates the voltage profile for the capacitive current response compared with the total measured current on a typical CV for **NNU-11** at a scan rate of 0.5 mV s^{-1}. The results showed that the capacitive-controlled capacity made up about 42.5% of the total capacity. Thus, a type of high-capacity LIBs, with these novel POMOFs with surface and diffusion-controlled lithium storage, was achieved.

EIS experiments of **NNU-11** were also carried out, and the spectra were simulated using the inset equivalent circuit (Fig. S12†). The Nyquist plots displayed a depressed semicircle and a straight line in the middle- and high-frequency region and low-frequency area respectively. R_1 corresponds to the electronic resistance of the electrodes and electrolyte, and the size of semicircles corresponds to the charge-transfer resistance (R_2). The straight line is allocated to the Warburg impedance (W_o) corresponding to the lithium diffusion process (Fig. S12†). As shown in Fig. S12,† **NNU-11** exhibited a distinctly smaller semicircle than other pristine POMOFs, and the total resistance was 56 Ω. However, the total resistance of **NNU-12** was 200 Ω, which is much higher than that of **NNU-11**, which indicates that the enhanced conductivity of **NNU-11** benefits from the electronic channels provided by the π–π stacking (Fig. 4b).[26]

The **NNU-11** electrode can be also reversibly cycled at various current densities of 50, 100, 200, 500 and 1000 mA g^{-1}, respectively (Fig. 3d). There is an increasing trend in the first few cycles for most of the samples, and this may be attributed to the activation of the electrodes and improvement during Li^+ insertion–deinsertion processes with repeated cycling. When the current density was reduced back to 50 mA g^{-1}, a capacity of 750 mA h g^{-1} was immediately resumed, which suggests good reversibility of the **NNU-11** electrode. Moreover, it exhibited good cycling stability at a higher current density of 500 mA g^{-1}. To fully activate the electrode, 50 mA g^{-1} was applied in the first ten cycles and 500 mA g^{-1} was carried out to run the long-cycle measurement. As shown in Fig. 3e, the **NNU-11** electrode exhibited a high reversible capacity of about 480 mA h g^{-1} at the beginning, which then gradually increased to 580 mA h g^{-1} after ~220 cycles. Finally, it maintained the capacity value of 480 mA h g^{-1} at 500 mA g^{-1} after the 400th cycle, and the capacity retention was 100.6% by comparing the capacity of the 400th cycle with the 11th cycle. This cycling stability is also among the best of the pristine MOFs based anodes that has ever been reported (Table S1†). SEM images of the electrode materials after cycling for 50 cycles at 500 mA g^{-1} and before cycling are seen in Fig. S13.† From Fig. S13a and b,† the formed SEI film can be seen clearly on the surface of the materials, and no cracking was observed. This may somehow explain the good stability of the **NNU-11** electrode.

Conclusion

In summary, we designed and synthesized an ultra-stable POMOF crystalline structure model supported by π–π stacking interactions, which contains $\{\varepsilon\text{-}PMo_8{}^{V}Mo_4{}^{VI}O_{40}Zn_4\}$ building blocks and TPT ligands. **NNU-11** exhibited outstanding stability in air and different organic solvents, even in different pH (pH 1–11) aqueous solutions. In addition, in virtue of consolidation of the multi-electron redox property of POM units and the functionalization of MOFs, **NNU-11** was employed as an anode material toward LIBs. **NNU-11** displayed reversible capacities of 750 mA h g^{-1} along with excellent cycle stability and rate performance, which is among the best of the pristine MOFs based anodes that were ever reported. These enhanced performances were attributed to the battery and capacitive behaviour. Intermolecular π–π stacking provides electrical path for electron transfer, which is beneficial to enhance the performance of LIBs. We employed the POMOF crystalline structure model with intermolecular π–π stacking interactions to demonstrate the interesting behaviour for the first time, which might guide the design and synthesis of advanced electrode materials based on nanomaterials for improving Li-storage.

Experimental section

Materials

All chemicals and reagents for syntheses were acquired from commercial sources. IR spectra using KBr pellets were recorded in the range of 4000–400 cm^{-1} on a Bruker Tensor 27 FT/IR spectrophotometer. Thermogravimetric analyses (TGA) were obtained at a heating rate of 10 °C min^{-1} under an oxygen atmosphere from room temperature to 700 °C on a Netzsch STA449F3 analyser. PXRD data were measured in the range of 3–50 °C on a D/max 2500VL/PC diffractometer equipped with graphite monochromatized Cu Kα radiation (λ = 1.54060 Å). All the spectra were calibrated by C 1s = 284.8 eV. X-ray photoelectron spectroscopy (XPS) utilizing Al Kα radiation was collected on scanning X-ray microprobe (PHI 5000 Verasa, ULAC-PHI, Inc.) using the C 1s peak at 284.8 eV as an internal standard.

Preparation of NNU-11

A mixture of $Na_2MoO_4{\cdot}2H_2O$ (310 mg, 1.28 mmol), $ZnCl_2$ (68 mg, 0.50 mmol), H_3PO_3 (10 mg, 0.125 mmol), tetrabutylammonium hydroxide 10 wt% solution in water (240 μL, 0.09 mmol), and H_2O (3.5 mL) was stirred for 10 min, and then the pH was adjusted to 1.0 with 2 M HCl solution. Subsequently, Mo powder 99.99% (25 mg, 0.26 mmol), TPT (46.85 mg, 0.15 mmol)

and appropriate DMA were added into the mixture of PH 1.0. Finally, the mixture was stirred for 30 min, sealed in a 15 mL Teflon-lined reactor and heated at 180 °C for 3 d. After cooling to room temperature, black plate crystals of **NNU-11** were collected (71% yield based on TPT) (Fig. S10†). IR (Fig. S8,† KBr pellets, ν/cm^{-1}): 1574 (w), 1516 (s), 1371 (s), 1312 (w), 1061 (w), 972 (m), 949 (m), 930 (m), 912 (m), 808 (m), 798 (m), 777 (m), 700 (w), 642 (m), 592 (m), 542 (w), 527 (w), 515 (w).

Single-crystal X-ray crystallography

Single-crystal XRD data for **NNU-11** and **NNU-12** were recorded on a Bruker APEXII CCD diffractometer with graphite-monochromatized Mo Kα radiation (λ = 0.71073 Å) at 296 K. Both were solved by SHELXT and refined by SHELXL-2014 within Olex^2. Except for hydrogen, all other atoms were refined with anisotropic temperature parameters. Hydrogen atoms from C atoms of TPT were located at calculated positions. For **NNU-12**, due to tetrabutylammonium ions and the water molecules disorder, the data was corrected with the program SQUEEZE, and a part of the PLATON software was utilized to check the space group of crystal. The detailed crystallographic information is summarized and shown in Table S2,† and some selected bond lengths are listed in Table S3.†

Electrochemical measurements

The crystal water of all the as prepared powders was removed before being used as the electrodes. 10 wt% polyvinylidene fluoride (PVDF), 20 wt% acetylene black (Super-P), and 70 wt% active material (**NNU-11**) were mixed in *N*-methyl-2-pyrrolidinone for preparing working electrodes. The electrodes that were coated on Cu foils using the above slurries were subsequently dried in vacuum for 6 h at 90 °C in order to eliminate the solvent. Then, before pressing, the above Cu foils were cut into disks (14 mm in diameter) and dried at 90 °C for one day in vacuum. Then, in an argon-filled glovebox under strictly controlled conditions the moisture and oxygen concentrations were limited to below 1 ppm, and the coin cells were laboratory-assembled by a CR 2032 press. A lithium foil and a Celgard 2400 membrane employed as the counter electrode and the separator, respectively. The electrolyte composition contained 1 M $LiPF_6$ in a mixture of dimethyl carbonate (DMC) and ethylene carbonate (EC) (v/v = 1 : 1). Finally, at various current densities of 50–1000 mA g^{-1} with a cut off voltage of 3–0.01 V *vs.* Li$^+$/Li, and the galvanostatic charge/discharge tests were carried out on a Land Battery Measurement System (Land, CT2001A, China) at room temperature. The specific capacity was calculated based on the mass of active material.

Acknowledgements

This study was financially supported by the National Natural Science Foundation of China (No. 21622104, 21371099 and 21471080), the NSF of Jiangsu Province of China (No. BK20141445), the Priority Academic Program Development of Jiangsu Higher Education Institutions and the Foundation of Jiangsu Collaborative Innovation Center of Biomedical Functional Materials and Jiangsu Planned Projects for Post-doctoral Research Funds (1601087C).

Notes and references

1 (*a*) M. Armand and J.-M. Tarascon, *Nature*, 2008, **451**, 652–657; (*b*) B. Dunn, H. Kamath and J. M. Tarascon, *Science*, 2011, **334**, 928–935; (*c*) R. W. Kates, W. C. Clark, R. Corell, J. M. Hall, C. C. Jaeger, I. Lowe, J. J. McCarthy, H. J. Schellnhuber, B. Bolin and N. M. Dickson, *Science*, 2001, **292**, 641–642.

2 (*a*) J.-M. Tarascon and M. Armand, *Nature*, 2001, **414**, 359–367; (*b*) G. Pagot, F. Bertasi, G. Nawn, E. Negro, G. Carraro, D. Barreca, C. Maccato, S. Polizzi and V. Di Noto, *Adv. Funct. Mater.*, 2015, **25**, 4032–4037; (*c*) T. Kazda, J. Vondrák, V. Di Noto, M. Sedlaříková, P. Čudek, L. Omelka, L. Šafaříková and V. Kašpárek, *J. Solid State Electrochem.*, 2015, **19**, 1579–1590; (*d*) V. Etacheri, R. Marom, R. Elazari, G. Salitra and D. Aurbach, *Energy Environ. Sci.*, 2011, **4**, 3243–3262.

3 (*a*) M. L. Aubrey and J. R. Long, *J. Am. Chem. Soc.*, 2015, **137**, 13594–13602; (*b*) P. Canepa, S. Jayaraman, L. Cheng, N. N. Rajput, W. D. Richards, G. S. Gautam, L. A. Curtiss, K. A. Persson and G. Ceder, *Energy Environ. Sci.*, 2015, **8**, 3718–3730; (*c*) D. A. Vazquez-Molina, G. S. Mohammad-Pour, C. Lee, M. W. Logan, X. Duan, J. K. Harper and F. J. Uribe-Romo, *J. Am. Chem. Soc.*, 2016, **138**, 9767–9770; (*d*) B. M. Wiers, M.-L. Foo, N. P. Balsara and J. R. Long, *J. Am. Chem. Soc.*, 2011, **133**, 14522–14525.

4 (*a*) A. Naji, P. Willmann and D. Billaud, *Carbon*, 1998, **36**, 1347–1352; (*b*) C. Menachem, Y. Wang, J. Flowers, E. Peled and S. Greenbaum, *J. Power Sources*, 1998, **76**, 180–185.

5 (*a*) E. Kang, Y. S. Jung, A. S. Cavanagh, G. H. Kim, S. M. George, A. C. Dillon, J. K. Kim and J. Lee, *Adv. Funct. Mater.*, 2011, **21**, 2430–2438; (*b*) S. Chen, Y. Xin, Y. Zhou, Y. Ma, H. Zhou and L. Qi, *Energy Environ. Sci.*, 2014, **7**, 1924–1930; (*c*) Y. Liu, Z. Cheng, H. Sun, H. Arandiyan, J. Li and M. Ahmad, *J. Power Sources*, 2015, **273**, 878–884; (*d*) N. Liu, H. Wu, M. T. McDowell, Y. Yao, C. Wang and Y. Cui, *Nano Lett.*, 2012, **12**, 3315–3321; (*e*) Y. Idota, T. Kubota, A. Matsufuji, Y. Maekawa and T. Miyasaka, *Science*, 1997, **276**, 1395–1397.

6 O. M. Yaghi, G. Li and H. Li, *Nature*, 1995, **378**, 703–706.

7 (*a*) S. Xiang, Y. He, Z. Zhang, H. Wu, W. Zhou, R. Krishna and B. Chen, *Nat. Commun.*, 2012, **3**, 954; (*b*) S. Qiu, M. Xue and G. Zhu, *Chem. Soc. Rev.*, 2014, **43**, 6116–6140.

8 (*a*) P. V. Dau and S. M. Cohen, *Inorg. Chem.*, 2015, **54**, 3134–3138; (*b*) T. Zhang, K. Manna and W. Lin, *J. Am. Chem. Soc.*, 2016, **138**, 3241–3249.

9 (*a*) S. Ma and H.-C. Zhou, *Chem. Commun.*, 2010, **46**, 44–53; (*b*) D. De, T. K. Pal, S. Neogi, S. Senthilkumar, D. Das, S. S. Gupta and P. K. Bharadwaj, *Chem.–Eur. J.*, 2016, **22**, 3387–3396; (*c*) P. Canepa, C. A. Arter, E. M. Conwill, D. H. Johnson, B. A. Shoemaker, K. Z. Soliman and T. Thonhauser, *J. Mater. Chem. A*, 2013, **1**, 13597; (*d*) L. Valenzano, B. Civalleri, K. Sillar and J. Sauer, *J. Phys. Chem. C*, 2011, **115**, 21777–21784; (*e*) L. Valenzano,

B. Civalleri, S. Chavan, G. T. Palomino, C. O. Areán and S. Bordiga, *J. Phys. Chem. C*, 2010, **114**, 11185–11191; (*f*) P. Canepa, N. Nijem, Y. J. Chabal and T. Thonhauser, *Phys. Rev. Lett.*, 2013, **110**, 026102.

10 (*a*) Z. Dou, J. Yu, Y. Cui, Y. Yang, Z. Wang, D. Yang and G. Qian, *J. Am. Chem. Soc.*, 2014, **136**, 5527–5530; (*b*) X. Z. Song, S. Y. Song, S. N. Zhao, Z. M. Hao, M. Zhu, X. Meng, L. L. Wu and H. J. Zhang, *Adv. Funct. Mater.*, 2014, **24**, 4034–4041.

11 (*a*) C. Wang, Z. Xie, K. E. deKrafft and W. Lin, *J. Am. Chem. Soc.*, 2011, **133**, 13445–13454; (*b*) J.-S. Qin, D.-Y. Du, W. Guan, X.-J. Bo, Y.-F. Li, L.-P. Guo, Z.-M. Su, Y.-Y. Wang, Y.-Q. Lan and H.-C. Zhou, *J. Am. Chem. Soc.*, 2015, **137**, 7169–7177.

12 X. Li, F. Cheng, S. Zhang and J. Chen, *J. Power Sources*, 2006, **160**, 542–547.

13 (*a*) K. Saravanan, M. Nagarathinam, P. Balaya and J. J. Vittal, *J. Mater. Chem.*, 2010, **20**, 8329–8335; (*b*) Q. Liu, L. Yu, Y. Wang, Y. Ji, J. Horvat, M.-L. Cheng, X. Jia and G. Wang, *Inorg. Chem.*, 2013, **52**, 2817–2822; (*c*) L. Gou, L.-M. Hao, Y.-X. Shi, S.-L. Ma, X.-Y. Fan, L. Xu, D.-L. Li and K. Wang, *J. Solid State Chem.*, 2014, **210**, 121–124.

14 (*a*) M. Vasilopoulou, A. M. Douvas, L. C. Palilis, S. Kennou and P. Argitis, *J. Am. Chem. Soc.*, 2015, **137**, 6844–6856; (*b*) R. E. Schreiber, H. Cohen, G. Leitus, S. G. Wolf, A. Zhou, L. Que and R. Neumann, *J. Am. Chem. Soc.*, 2015, **137**, 8738–8748.

15 Z. Luo, P. Kögerler, R. Cao and C. L. Hill, *Inorg. Chem.*, 2009, **48**, 7812–7817.

16 (*a*) H. Wang, S. Hamanaka, Y. Nishimoto, S. Irle, T. Yokoyama, H. Yoshikawa and K. Awaga, *J. Am. Chem. Soc.*, 2012, **134**, 4918–4924; (*b*) J. J. Chen, M. D. Symes, S. C. Fan, M. S. Zheng, H. N. Miras, Q. F. Dong and L. Cronin, *Adv. Mater.*, 2015, **27**, 4649–4654.

17 (*a*) Y. Yue, Y. Li, Z. Bi, G. M. Veith, C. A. Bridges, B. Guo, J. Chen, D. R. Mullins, S. P. Surwade and S. M. Mahurin, *J. Mater. Chem. A*, 2015, **3**, 22989–22995; (*b*) X. Xu, S. Chen, Y. Chen, H. Sun, L. Song, W. He and X. Wang, *Small*, 2016, **12**, 2982–2990.

18 (*a*) J. Y. Koo, Y. Yakiyama, G. R. Lee, J. Lee, H. C. Choi, Y. Morita and M. Kawano, *J. Am. Chem. Soc.*, 2016, **138**, 1776–1779; (*b*) G. Wu, J. Huang, Y. Zang, J. He and G. Xu, *J. Am. Chem. Soc.*, 2017, **139**, 1360–1363.

19 (*a*) L. Zhang, X. Kuang, X. Wu, W. Yang and C. Lu, *Dalton Trans.*, 2014, **43**, 7146–7152; (*b*) B.-Q. Song, X.-L. Wang, C.-Y. Sun, Y.-T. Zhang, X.-S. Wu, L. Yang, K.-Z. Shao, L. Zhao and Z.-M. Su, *Dalton Trans.*, 2015, **44**, 13818–13822.

20 (*a*) W. Guo, X. Tong and S. Liu, *Electrochim. Acta*, 2015, **173**, 540–550; (*b*) Y. Liu, S. Liu, X. Lai, J. Miao, D. He, N. Li, F. Luo, Z. Shi and S. Liu, *Adv. Funct. Mater.*, 2015, **25**, 4480–4485; (*c*) P. Huo, M. Zhou, Y. Tang, X. Liu, C. Ma, L. Yu and Y. Yan, *J. Alloys Compd.*, 2016, **670**, 198–209.

21 J. Xie, Y. Zhang, Y. Han and C. Li, *ACS Nano*, 2016, **10**, 5304–5313.

22 B. Dasgupta, Y. Ren, L. M. Wong, L. Kong, E. S. Tok, W. K. Chim and S. Y. Chiam, *J. Phys. Chem. C*, 2015, **119**, 10592–10601.

23 K. Yasakau, I. Giner, C. Vree, O. Ozcan, R. Grothe, A. Oliveira, G. Grundmeier, M. Ferreira and M. Zheludkevich, *Appl. Surf. Sci.*, 2016, **389**, 144–156.

24 Y. Nishimoto, D. Yokogawa, H. Yoshikawa, K. Awaga and S. Irle, *J. Am. Chem. Soc.*, 2014, **136**, 9042–9052.

25 (*a*) T. Yuan, Y. Jiang, W. Sun, B. Xiang, Y. Li, M. Yan, B. Xu and S. Dou, *Adv. Funct. Mater.*, 2016, **26**, 2198–2206; (*b*) P. Simon, Y. Gogotsi and B. Dunn, *Science*, 2014, **343**, 1210–1211; (*c*) M. R. Lukatskaya, B. Dunn and Y. Gogotsi, *Nat. Commun.*, 2016, **7**, 12647; (*d*) V. Augustyn, P. Simon and B. Dunn, *Energy Environ. Sci.*, 2014, **7**, 1597–1614; (*e*) J. Wang, J. Polleux, J. Lim and B. Dunn, *J. Phys. Chem. C*, 2007, **111**, 14925–14931.

26 (*a*) Q.-C. Zhuang, T. Wei, L.-L. Du, Y.-L. Cui, L. Fang and S.-G. Sun, *J. Phys. Chem. C*, 2010, **114**, 8614–8621; (*b*) B. Liu, X. Zhao, Y. Xiao and M. Cao, *J. Mater. Chem. A*, 2014, **2**, 3338–3343.